




RESEARCH ARTICLE | MARCH 21 2023

Heat transfer to proximal cylinders in hypersonic flow

Special Collection: [Hypersonic Flow](#)

Monal Patel ; Salvador Navarro-Martinez  



Physics of Fluids 35, 036125 (2023)

<https://doi.org/10.1063/5.0137905>



Articles You May Be Interested In

Sustainable space technologies—Strategies toward a predictive aerothermal design of re-useable space transportation systems

Rev. Sci. Instrum. (February 2024)

Aerothermal optimization of turbine cascade squealer tip with non-uniform squealer height

Physics of Fluids (November 2023)

Effects of rotor squealer tip with non-uniform heights on heat transfer characteristic and flow structure of turbine stage

Physics of Fluids (November 2024)



Physics of Fluids

Special Topics Open
for Submissions

[Learn More](#)

Heat transfer to proximal cylinders in hypersonic flow

Cite as: Phys. Fluids **35**, 036125 (2023); doi: [10.1063/5.0137905](https://doi.org/10.1063/5.0137905)

Submitted: 6 December 2022 · Accepted: 3 March 2023 ·

Published Online: 21 March 2023



View Online



Export Citation



CrossMark

Monal Patel^{a)}  and Salvador Navarro-Martinez^{b)} 

AFFILIATIONS

Department of Mechanical Engineering, Imperial College London, London SW7 2AZ, United Kingdom

Note: This paper is part of the special topic, Hypersonic Flow.

^{a)}Electronic mail: monal.patel12@imperial.ac.uk

^{b)}Author to whom correspondence should be addressed: s.navarro@imperial.ac.uk

ABSTRACT

Uncontrolled atmospheric entry of meteors, satellites, and spacecraft components often leads to their partial or complete demise. In this destructive process, driven by hypersonic ablation, reentry objects fragment, interact, and alter each other's aerothermal environment. The effect of these interactions on the heat transfer to the fragments has not been investigated, despite the heat transfer's importance in hypersonic ablation and reentry demise. This study focuses on the numerical investigation of heat transfer to proximal circular cylinders in a thermochemically frozen flow and in two dimensions. First, binary body configurations at Mach numbers 2, 4, and 8 revealed that the heat load and peak heat transfer can be augmented for either or both proximal bodies by +20% to −90% of an isolated body. Second, different clusters of five proximal bodies showed that the heat load to any given body can range from +40% to −90% of an isolated body. Moreover, the average heat load in a cluster is found to vary between +20% and −60% of an isolated body. Intuitively, clusters which are thin in the direction perpendicular to free-stream velocity and long in the direction parallel to the free-stream velocity have their cluster-averaged heat load reduced. In contrast, thick and thin clusters, in directions perpendicular and parallel to the free-stream velocity, are subject to an increased cluster-averaged heat load.

© 2023 Author(s). All article content, except where otherwise noted, is licensed under a Creative Commons Attribution (CC BY) license (<http://creativecommons.org/licenses/by/4.0/>). <https://doi.org/10.1063/5.0137905>

I. INTRODUCTION

Uncontrolled atmospheric entry often results in fragmentation and partial or complete ablation of the entry body. The fragments formed during the entry can interact, altering each other's aerothermal environment. Such interactions occur in meteor entries¹ and are known to affect their trajectories and ground dispersion.² Moreover, discarded spacecraft components and whole satellites³ also fragment during reentry, and their demise is also likely to be affected by the fragment interactions. Motivated by these applications, several studies of proximal body interactions in hypersonic flow have emerged in the last 15 years. These studies have focused on aerodynamic forces, and aerothermal heating has not been investigated, despite its importance in reentry body demise. However, studies^{4–6} have investigated extreme localized heating due to shock-interactions, which can occur over complex surfaces or in certain proximal body arrangements. Nevertheless, these studies do not contribute significantly toward the understanding of the aerothermal environment during atmospheric entry demise.

One of the first studies on proximal body interactions by Laurence *et al.*⁷ experimentally and computationally investigated the forces on binary proximal cylinders and spheres in fixed positions, specifically when the second body was entirely within the primary body's shock layer. First, they developed an analytical theory based on the blast wave analogy and validated it experimentally and numerically. They found that the secondary body experiences not only a drag force but also a lift force. This lift force is exclusively attractive toward the second body if its diameter is larger than one-sixth of the primary body. This follows the intuition of the secondary body being pulled behind the primary body and becoming trapped in its wake. More recently, Marwege *et al.*⁸ developed a data-driven method for calculating forces in binary proximal body interactions with an accuracy within a few percent of numerical simulations.

Another early study by Laurence *et al.*⁹ investigated the dynamic separation of two, initially attached, spheres. They classified three main behaviors depending on the size and position of the detaching body. First, expulsion from the bow shock layer, which occurs with

increasing size ratios and detachment position toward the front stagnation point. It results in the secondary body being permanently excluded from the primary body’s bow shock. Second is shock surfing,¹⁰ where at a critical angle for a given radii ratio, the detached body follows the primary body’s bow shock downstream. Third is entrainment in bow shock, where moving the detachment position toward the rear centerline increases the probability of the secondary body being entrained within the primary body’s bow shock.

Moreover, several recent studies expand on the initial studies. For example, Park *et al.*¹¹ experimentally investigated the separation behavior of cubes and rough spheres. They noted that the body shape, surface roughness, and rotational motion affected the separation velocity. Furthermore, Park and Park,¹² Whalen and Laurence¹³ experimentally studied sphere clusters as large as 36 spheres and found that larger clusters separate faster than smaller ones. Similarly, Sousa *et al.*,¹⁴ Butler *et al.*¹⁵ experimentally and computationally investigated the dynamics of a spherical body shedding from a hypersonic ramp.

The literature suggests the possibility of persisting proximal body interactions during reentry, as the fragmented bodies could be trapped in the parent body’s bow shock during entry. Despite this, aerothermal heating in proximal bodies during atmospheric entry has not been investigated. As a first study focusing on heat transfer, this work aims to investigate the heat transfer to proximal circular cylinders in frozen and two-dimensional hypersonic flow.

This paper is organized as follows: Sec. II reviews the relevant flow physics; Sec. III describes the governing equations and computational method; Sec. IV investigates the heat transfer with binary proximal bodies; Sec. V investigates the heat transfer to multiple proximal bodies; and finally, Sec. VI concludes the study.

II. FLOW PHYSICS

A. Hypersonic blunt body wake

Hypersonic blunt body wakes consist of a rotational inviscid shock layer, a viscous inner wake and various shock and expansion waves. Many studies have investigated blunt body hypersonic near wakes, see the introduction in Hinman and Johansen,¹⁶ whereas less is known about far hypersonic wakes.^{17–19} The key features and length scales in hypersonic wakes are illustrated in Fig. 1. The bow shock around the blunt body drastically slows the flow to subsonic speeds around the front of the cylinder. A boundary layer starts from the front stagnation point and remains attached for larger turn angles compared to subsonic flows due to the favorable pressure gradient created by the expansion fan. However, adverse pressure gradients eventually form and separate the boundary layer, resulting in a separation shock—also known as a lip shock.²⁰ The separated flow converges toward the wake centerline at the reattachment point, where some flow is directed back to create a counter-rotating vortex pair near the base. With an increasing Reynolds number, the re-circulation may have more than one vortex pair. The flow that continues away from the body along the centerline creates a reattachment shock and forms a viscous inner wake which may transition to turbulence and mix with the inviscid shock layer downstream. The flow field is symmetrical along the centerline for symmetric blunt bodies, but the symmetry breaks as the wake transitions to turbulence.

Wake Reynolds number (Re_w) governs the wake topology,

$$Re_w = \frac{\rho_d u_d h}{\mu_d}, \tag{1}$$

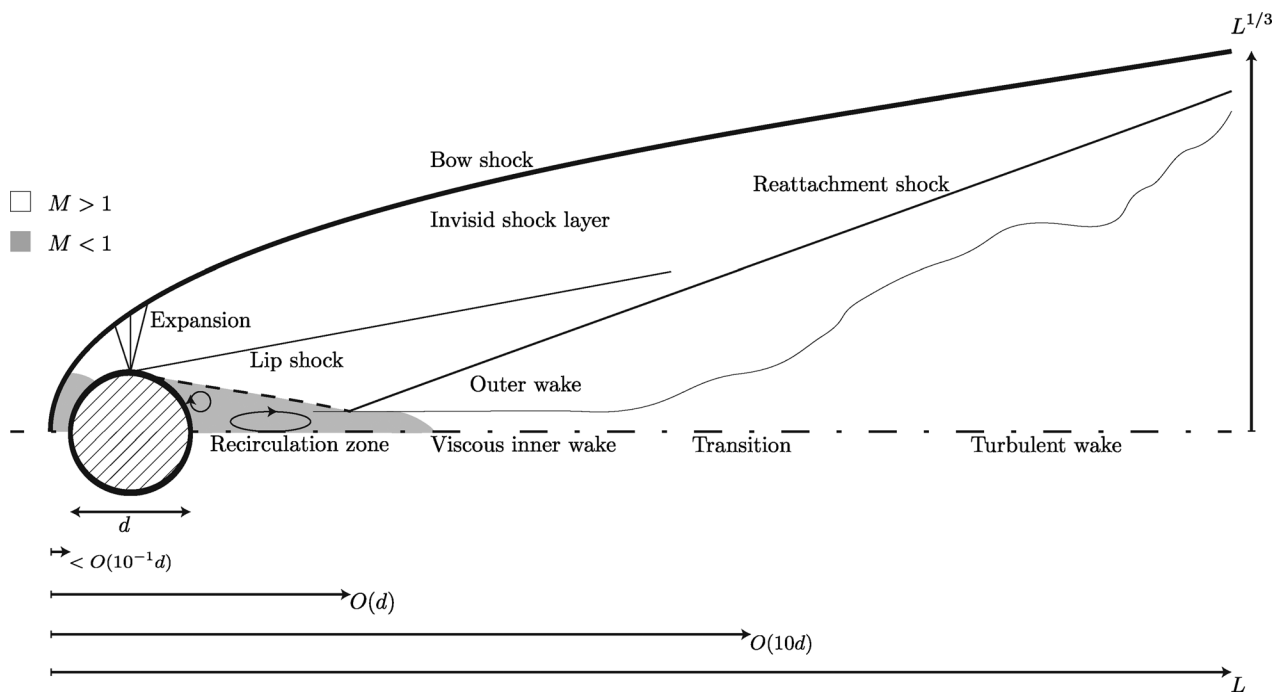


FIG. 1. Hypersonic blunt body wake flow features with approximate length scales.

02 January 2025 11:35:46

where h is the wake base height, the shortest distance between the separation point and the centerline. Semi-analytical expressions for calculating the dividing streamline density (ρ_d), temperature and viscosity (μ_d) can be found in Eqs. 3.1–3.7 from Hinman and Johansen.¹⁶ Although a more convenient scaling parameter is the free-stream Reynolds number, Re_∞ , which is based on free-stream flow properties and body length scale. It is not useful in describing the wake behavior as it does not account for the flow features that occur upstream of the wake. Figure 2 shows the relationship between the two Reynolds numbers and free-stream Mach number, M_∞ , without thermochemical effects. It shows that generally $Re_w \ll Re_\infty$, and that increasing M_∞ for a given Re_∞ , reduces Re_w due to increasing temperature and viscosity. Moreover, it outlines four flow regimes: A is diffusion-dominated, essentially Stokes flow; B—where the re-circulation region changes from diffusion to convection-dominated; C—where the wake is convection dominated and maybe unsteady; and D—where the wake is convection dominated and will transition to a turbulent wake.

B. Stagnation-point and shock-interaction heat transfer

Stagnation-point heat transfer is governed by the exact solution of compressible boundary layer equations.²¹ For frozen flow around a cylinder, the stagnation heat flux is

$$q_0 = 0.57Pr^{-0.6}(\rho_e\mu_e)^{1/2}\sqrt{\frac{du_e}{d\xi}}(h_{aw} - h_w), \quad (2)$$

$$\frac{du_e}{d\xi} \approx \frac{1}{R}\sqrt{\frac{2(P_e - P_\infty)}{\rho_e}}, \quad (3)$$

where q_0 is the stagnation-point heat flux, Pr is the Prandtl number, ρ_e is the boundary layer edge density, μ_e is the boundary layer edge viscosity, h_{aw} is adiabatic wall enthalpy, h_w is the wall enthalpy, and $du_e/d\xi$ is the velocity gradient in the wall tangent direction (ξ) at the boundary layer edge. A similar expression with chemically reacting

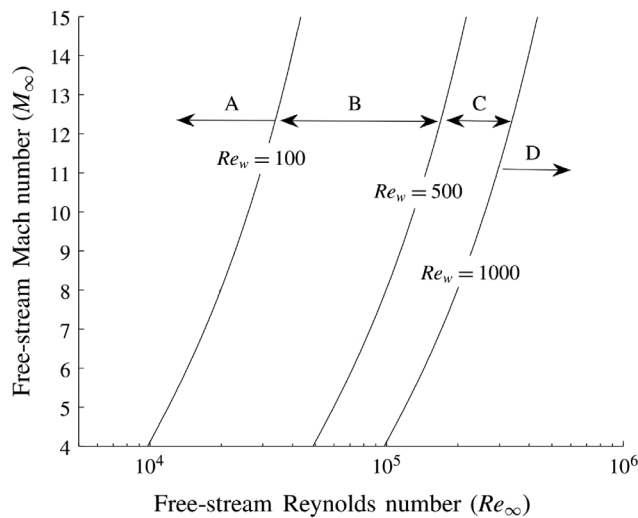


FIG. 2. Relationship between wake Reynolds number (Re_w), free-stream Reynolds number (Re_∞), and free-stream Mach number (M_∞). Adapted from Ref. 16.

flows is not shown here as current work assumes frozen flow. The velocity gradient can be approximated using Newtonian theory,²² as in Eq. (3), where R is the nose radius, P_∞ is the free-stream pressure, and P_e and ρ_e are boundary layer edge pressure and density.

There are many simplified forms of Eq. (2) and are reviewed by Tauber,²³ where they state a simple expression for cylinders:

$$q_0 = 1.29 \times 10^{-4} \left(\frac{\rho_\infty}{R}\right)^{0.5} V_\infty^3 \left(1 - \frac{h_w}{h_{aw}}\right). \quad (4)$$

They also state that the distribution of surface heat transfer is approximately

$$q_w = q_0 \cos(\theta)(1 - 0.18 \sin^2(\theta)), \quad (5)$$

$$h_{aw} = h_\infty + 1/2V_\infty^2(1 - 0.18 \sin^2(\theta)),$$

where θ is the position angle on the cylinder surface. Assuming $h_{aw} \gg h_w$, Eq. (4) can also be written in terms of non-dimensional flow parameters, free-stream temperature and the length scale,

$$q_0 \propto R^{-1} Re_\infty^{1/2} M_\infty^{5/2} T_\infty^{5/4}, \quad (6)$$

where C is a constant which includes free-stream fluid properties, namely, specific heats' ratio, gas constant and viscosity. Expression (6) scales with $Re_\infty^{1/2}$ and $M_\infty^{5/2}$ assuming the wall temperature is much colder than the stagnation temperature.

Shock interaction heating occurs when an impinging shock interacts with the body's bow shock near its surface. These interactions can be decomposed into six canonical flow patterns, as initially described by Edney.⁵ Types I, II, and V are associated with a shock-boundary-layer interaction; type III is characterized by an attaching free shear layer; type IV is characterized by an impinging or grazing supersonic jet; and type VI by an expansion-fan-boundary-layer interaction. Only type VI results in a reduction of surface gradients and pressure, all other types result in an increase in local pressure and surface gradients. Most severe heating generally occurs when a shock or a shear layer impinges on the body surface and can lead to $10\times$ nominal heating or even higher.⁶ Typically, this increase in heating also correlates with an increase in surface pressure of a similar magnitude.

Semi-empirical heat transfer correlations have been developed for each type of interaction by Keyes and Hains.⁶ The exact equations are not shown here for brevity, but the correlations suggest that all types of interactions strongly depend on the impinging and bow shock angles at the intersection; as well as the local surface inclination and interaction-specific flow length scale.

III. NUMERICAL METHOD

This work uses a Navier–Stokes computational fluid dynamics solver, originally designed for modeling reacting and dense compressible fluids.^{24,25} More recently, the solver has been further developed with a focus on modeling hypersonic flows.²⁶ It has been coupled with BoxLib,²⁷ a structured Cartesian adaptive mesh refinement massively parallel framework and a ghost-point forcing immersed boundary method. The solver has been validated over a range of test cases with a focus on surface properties predictions (pressure, velocity gradients, and temperature gradients). The tests include stand-off and surface pressure predictions up to sub-orbital Mach numbers ($M \leq 30$) in Euler flow. In addition to pressure, heat transfer and skin friction predictions over compression ramp with shock-shock and

shock–boundary layer interactions in viscous flow. The solver is well suited for resolving a large range of flow scales, often found in hypersonic flows, and modeling flows around complex geometries.

The solver computes the Navier–Stokes equations conservation laws as follows:

$$\frac{\partial}{\partial t} \begin{pmatrix} \rho \\ \rho \mathbf{u} \\ \rho e_t \end{pmatrix} + \nabla \cdot \begin{pmatrix} \rho \mathbf{u} \\ \rho \mathbf{u} \otimes \mathbf{u} + p \mathbf{I} \\ \rho u h_t \end{pmatrix} + \nabla \cdot \begin{pmatrix} 0 \\ -\boldsymbol{\tau} \\ \mathbf{q} - \boldsymbol{\tau} \cdot \mathbf{u} \end{pmatrix} = \mathbf{0}, \quad (7)$$

$$\boldsymbol{\tau} = \mu \left(\nabla \mathbf{u} + (\nabla \mathbf{u})^T - \frac{2}{3} \nabla \cdot \mathbf{u} \mathbf{I} \right), \quad \mathbf{q} = -\lambda \nabla T,$$

where ρ is the density, \mathbf{u} is the velocity vector, p is the pressure, e_t is the total energy, \mathbf{I} is the identity matrix, ∇ is the gradient operator, h_t is the total enthalpy, $\boldsymbol{\tau}$ is the shear stress tensor, μ is the dynamic viscosity, \mathbf{q} is the thermal conduction flux vector, and λ is the thermal conductivity. The Euler fluxes are calculated via a fourth-order accurate central-skew-like conservative difference method with artificial dissipation shock-capturing.²⁸

The viscous fluxes are computed with second-order accurate standard central difference. The time integration is with a local time-stepping strategy in the AMR framework—where the time step is halved, and the number of steps doubled, for each refinement level to maintain a constant Courant–Friedrichs–Lewy (CFL) number on all refinement levels in uniform flow. Equation (7) is time-marched with an explicit third-order total variation diminishing Runge–Kutta scheme.²⁹ In closing Eq. (7), the following assumptions are made: N_2 gas free-stream, frozen flow, Sutherland’s law viscosity, constant specific heat capacity ($c_p = 1040 \text{ kJ/kg K}$), and constant Prandtl number ($Pr = 0.7$).

Previous numerical studies focusing on proximal body separation^{7,9} have used computational methods similar to the current work: combining a high-order shock-capturing method with embedded ghost-cell boundary conditions and parallel dynamically adaptive structured Cartesian meshes.

IV. BINARY BODIES

An expression for the transverse velocity (V_t) of proximal spherical bodies was first presented by Passey and Melosh,² which was later verified further by dynamical separation studies of Laurence *et al.*⁹ and Park *et al.*¹¹ The expression reads

$$\frac{V_t}{V_\infty} = \sqrt{C \frac{r_1 \rho_\infty}{r_2 \rho_b}}, \quad r_2 \leq r_1, \quad (8)$$

where C is a constant, r_1 and r_2 are radii of the two spherical bodies, ρ_∞ is free-stream density, V_∞ is free-stream velocity, and ρ_b is the density of the detached body. The order of magnitudes for each variable considering Earth entries are as follows. The constant C , as discussed by Laurence *et al.*,⁹ is $10^{-2} < O(C) < 1$. The number of fragments are assumed to be small, so $O(n) = 1$. The fragmented bodies are assumed to be smaller than the primary body but not too small, which means $10^{-1} < (r_1/r_2) < 1$. Finally, the ratio of the free-stream density to body density is not trivial. Spacecraft components and satellites are usually metallic, and common meteorites³⁰ are stony, stony-iron, or iron. A reasonable assumption is to consider a metallic body, so $O(\rho_b) = 10^3 \text{ kg/m}^3$. Passey and Melosh² suggest that breakup altitudes can be as low as 6 km and as high as the mesosphere (approximately 80 km), so $10^{-5} < O(\rho_\infty) < 1 \text{ kg/m}^3$. Therefore, $10^{-6} < O(V_t/V_\infty) < 10^{-1}$;

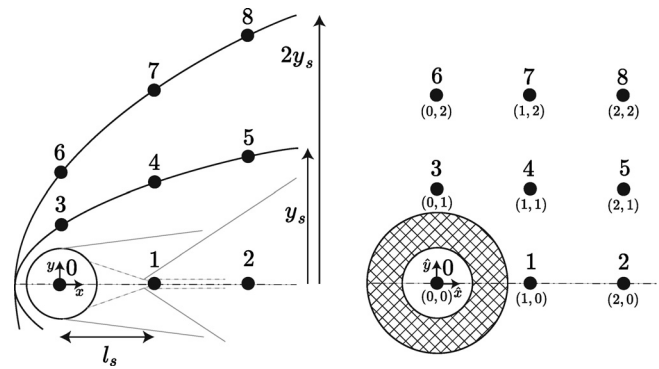


FIG. 3. Binary bodies arrangements in real (left) and non-dimensional (right) space.

this suggests that the separation velocity varies over orders of magnitude and is much slower than free-stream velocity. Therefore, the flow adjusts very quickly around the bodies and neglecting body dynamics can be justified as a first approximation.

In this work, two identical bodies with 0.1 m diameter are considered. The body positions are non-dimensionalized using flow length scales, instead of the body length scale, as it allows a meaningful comparison of positions across different Mach numbers. The positions in real space (x, y) and non-dimensional space (\hat{x}, \hat{y}) are illustrated in Fig. 3. The figure also shows a hatched region representing a collision area where the second body cannot be placed. The second body’s position is systematically varied in the primary body’s near wake, $0 \leq \hat{x} \leq 2$ and $0 \leq \hat{y} \leq 2$. The reference length scale in the y direction is the shock radius (y_s) and in the x direction is the rear stagnation-point distance (l_s) from the body center. The different positions are investigated at Mach numbers 2, 4, and 8. These Mach numbers are lower than typical atmospheric entry flows, which could be up to Mach 30, where thermochemical relaxation and radiative heat transfer have a significant effect on the overall heat transfer. Including these physical phenomena is beyond the scope of the current work, and therefore, the conditions investigated are representative of low altitude conditions. The free-stream Reynolds number is fixed at 10 000, and the free-stream temperature is 300 K. Therefore, the flow is completely characterized by the Mach number. The wall temperature is 300 K for Mach 2 and 500 K for the other two conditions. The wake Reynolds numbers are less than 100 for the free-stream Reynolds and Mach numbers, suggested by Fig. 2, and laminar flow behavior is expected.

A. Mesh refinement

A mesh refinement study is conducted at the three Mach numbers, from which the meshes are summarized in Table I. The Mach 2

TABLE I. Mesh refinement cases with low, medium, and high resolutions for each Mach number. For each mesh, the number of computational points ($\times 10^6$) and the number of refinement levels in brackets are shown.

M	Size	Base	Low	Medium	High
2	20D × 20D	2048 × 2048	4.60 (2)	4.88 (3)	5.12 (4)
4	10D × 10D	1024 × 1024	1.34 (2)	1.45 (3)	1.66 (4)
8	10D × 10D	2048 × 2048	5.31 (4)	6.18 (5)	7.50 (6)

mesh has more number of computational points than the Mach 4 because a larger domain is required due to the wider shock layer. The mesh requirement for accurate stagnation-point heat transfer prediction can be estimated using Eq. (4). Figures 4(a) and 4(b) show the mesh in a fully developed flow field, with refinement around shock and cylinder boundary at $M = 4$, and with refinement around the cylinder boundary only at $M = 8$. The mesh for $M = 2$ is similar and not shown for brevity. At $M = 8$, the higher levels of refinement (3, 4, and 5) are added around the front of the cylinder using criteria based on the wall pressure coefficient. The simulations are initialized at the free-stream temperature and pressure with free-stream Mach number everywhere except for a small annulus around the cylinder, where the Mach number is zero. The domain boundary conditions, considering Fig. 4, are free-stream inflow on the left boundary and zero-gradient for all other boundaries. For the immersed boundary, no-slip, constant wall temperature and zero pressure gradient conditions are imposed. The simulations are computed for 10 flow times, where a flow time is defined as the domain length divided by the free-stream velocity. The maximum CFL number is around 0.5. Re-gridding occurs every 0.5 flow times. The flow length scales required for the non-dimensionalization are computed from the mesh refinement results and are listed in Appendix A.

The non-dimensional surface properties, pressure (C_p), skin friction (C_f), and heat transfer (C_h) coefficients are defined as follows:

$$C_p = \frac{P_w}{1/2\rho_\infty u_\infty^2}; \quad C_f = \frac{\tau_w}{1/2\rho_\infty u_\infty^2}; \quad C_h = \frac{q_w}{1/2\rho_\infty u_\infty^3}. \quad (9)$$

Figure 5 shows surface properties down-sampled to 100 surface elements and averaged with a three-point moving filter. The pressure field does not vary significantly with increasing resolution at all Mach numbers. The reference (Ref) heat transfer profile is from Eq. (5), which are known to include around 25% error when compared to ground shock-tube and ballistic range experiments.²³ The stagnation-point heat transfer predictions from all meshes are within this error. Table II suggests that at $M = 2$, the stagnation heat transfer is over-predicted by 10%. At $M = 4$ and 8, the stagnation heat transfer is under-predicted by around 10%. Another observation is that the heat transfer profile qualitatively agrees but is offset around a factor of the stagnation-point heat transfer error, and it does not agree well beyond $3\pi/8$ as expected. For all Mach numbers, the medium mesh resolution gives results within 3% of the fine mesh results; therefore, it is deemed acceptable for binary bodies computations.

B. Results

Initial studies suggested secondary body arrangements with $\hat{y} = 2$ were too far to observe any effect on each other. So, despite the illustration in Fig. 3, the study is limited to $\hat{y} \leq 1$. Eight arrangements of the

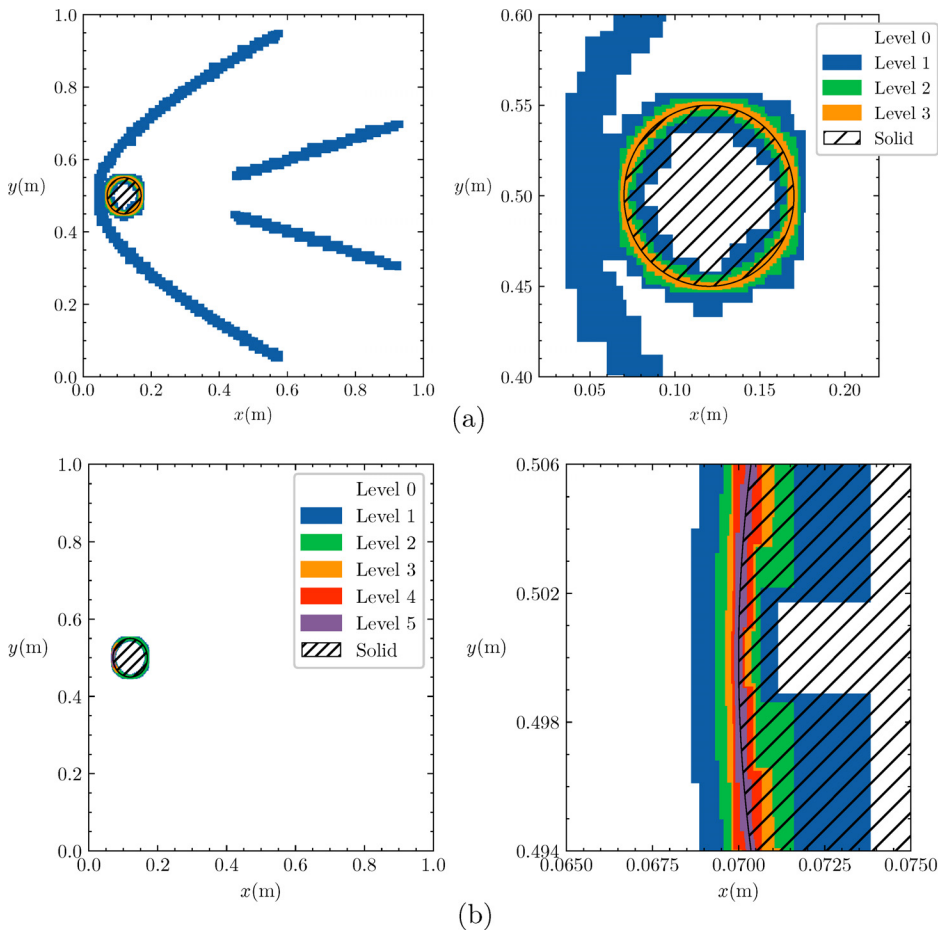


FIG. 4. Medium resolution AMR mesh at Mach numbers 4 and 8. (a) At $M = 4$, left is the entire mesh and right is the zoomed mesh around the body. (b) At $M = 8$, left is the entire mesh and right is zoomed mesh around stagnation point.

02 January 2025 11:35:46

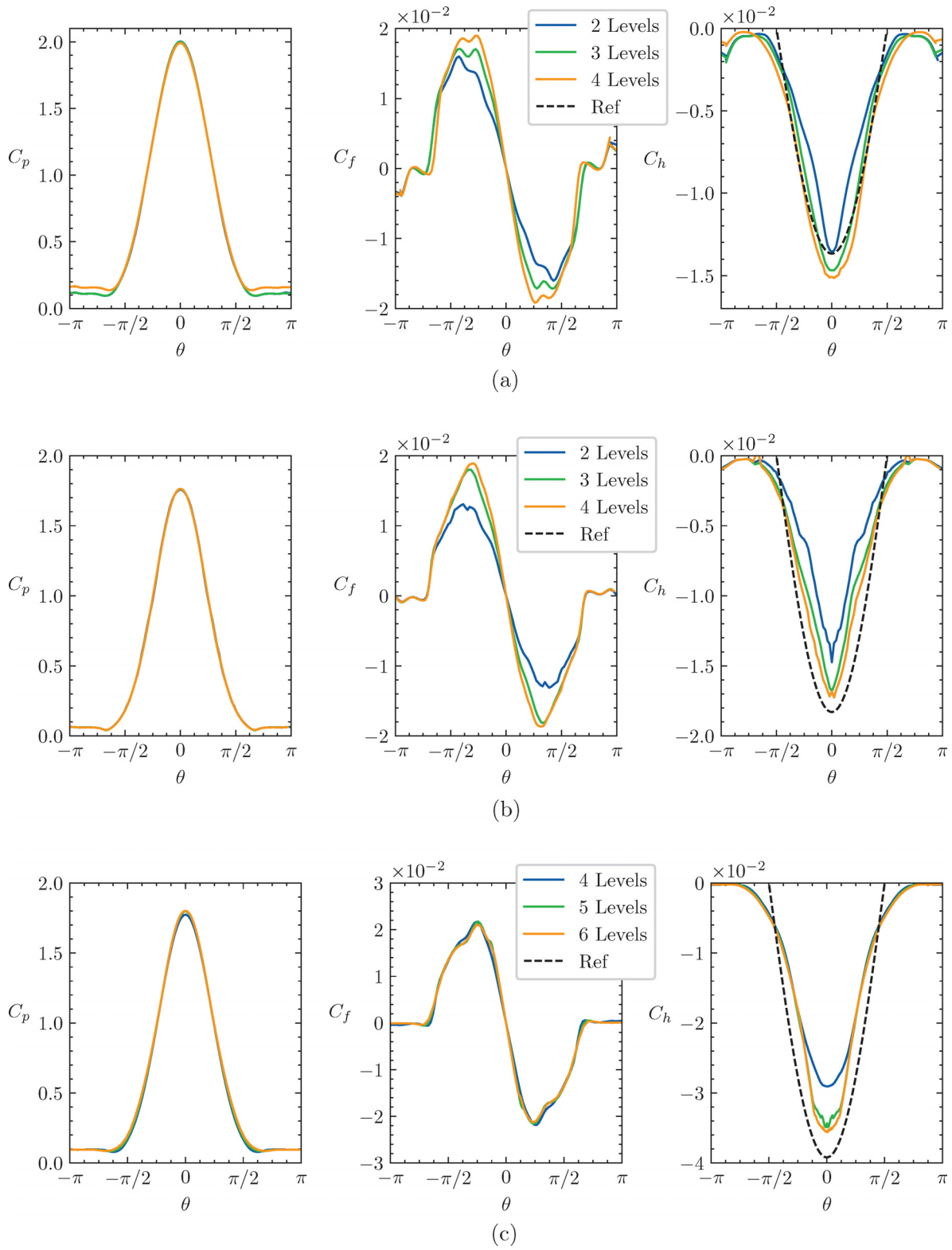


FIG. 5. Surface properties from mesh refinement study at different Mach numbers.

02 January 2025 11:35:46

TABLE II. Stagnation point heat transfer convergence (C_h) with increasing Mesh resolution at different Mach numbers and comparison with semi-empirical correlations of Tauber.²³

M	$ C_h \times 10^{-2}$						
	Low	Change (%)	Medium	Change (%)	High	Difference (%)	Reference
2	1.36	8.1	1.47	2.7	1.51	10.2	1.37
4	1.47	14.2	1.68	3.0	1.73	-5.4	1.83
8	2.91	20.0	3.49	2.0	3.56	-9.2	3.92

bodies are considered, in (\hat{x}, \hat{y}) coordinates and in order from 1 to 8 are $\{(1,0), (2,0), (0,0.5), (1,0.5), (2,0.5), (0,1), (0.5,1), \text{ and } (1,1)\}$. Simulations are conducted using these arrangements and the numerical setup is identical to the medium mesh simulations from the refinement study in Sec. IV A, but with two immersed bodies. The meshing criteria around both bodies are the same. The simulations are advanced for 10 flow-through times; this duration is sufficient for the surface gradients to be developed close to a steady state, as shown in Fig. 6. The figure shows the heat load variation of primary and secondary bodies with non-dimensional time. The heat load is more unsteady at lower Mach numbers but only for a couple of arrangements. Specifically, at $M=2$ in arrangements 2 and 4, and at $M=4$ in arrangements 2 and 5. Therefore, the surface properties for these cases are time-averaged over 5–10 flow times, but for all other cases, the surface properties are taken at their steady state.

The typical mesh contains around $[4.6, 1.5, 5.6] \times 10^6$ points for Mach numbers [2, 4, 8]. In all the meshes, more than 80% of

computational points are on the base level. Each binary body arrangement costs around [980, 170, 1590] CPU hours to compute. The $M=2$ mesh is almost the same size as the $M=8$ mesh as the lower Mach number domain is twice as large and the base mesh resolution is the same for both Mach numbers.

1. Numerical Schlieren

Figures 7–9 show similar flow features to Fig. 1, namely bow shock, lip shock, and reattachment shocks. In arrangements 1 and 2 for all Mach numbers, the secondary body does not have a bow shock when directly behind the primary body. In arrangements 3–8, both bodies have interacting bow shocks. In arrangements 3, 6, and 7 at $M=2, 3,$ and 6 for $M=4$ and only in arrangement 6 at $M=8$; the bow shocks combine and form a single smooth bow shock, or they result in interactions which can lead to unsteady wakes with oscillating reattachment shocks and shocklet shedding. Counter-intuitively, the wake becomes more steady at increasing Mach numbers. This is because the wake behavior is governed by the wake Reynolds number which decreases with increasing free-stream Mach number for a fixed free-stream Reynolds number, as shown in Fig. 2.

The results show Edney-type shock interactions but mostly far from the body surface. They are known to occur with near-body shock interactions, as discussed in Sec. II B. However, most of the binary body arrangements are such that the secondary body is positioned fully inside the shock layer of the primary body. This is the case at $M=2$ and $M=4$ for all arrangements; and at $M=8$ with arrangements 1, 2, 6, and 7. Therefore, in these arrangements, there is no impinging shock and bow shock interaction. Arrangements 3, 4, 5, and 8 at $M=8$ are close to producing Edney-type interactions.

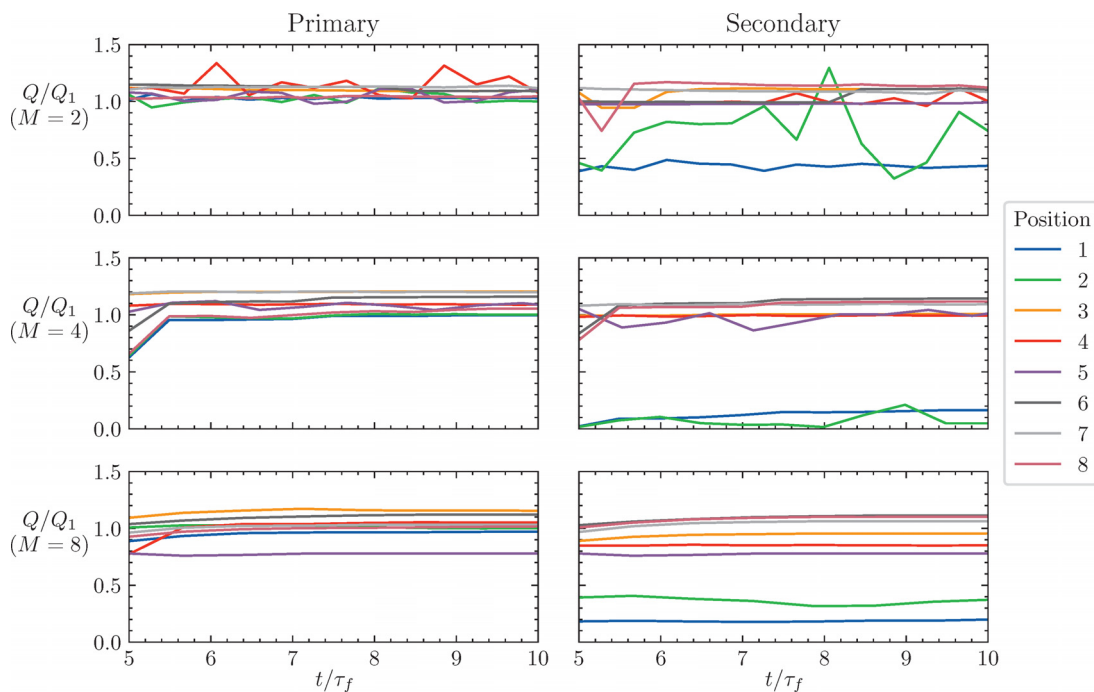


FIG. 6. Heat load variation for all arrangements and Mach numbers 2, 4, and 8, with non-dimensional time.

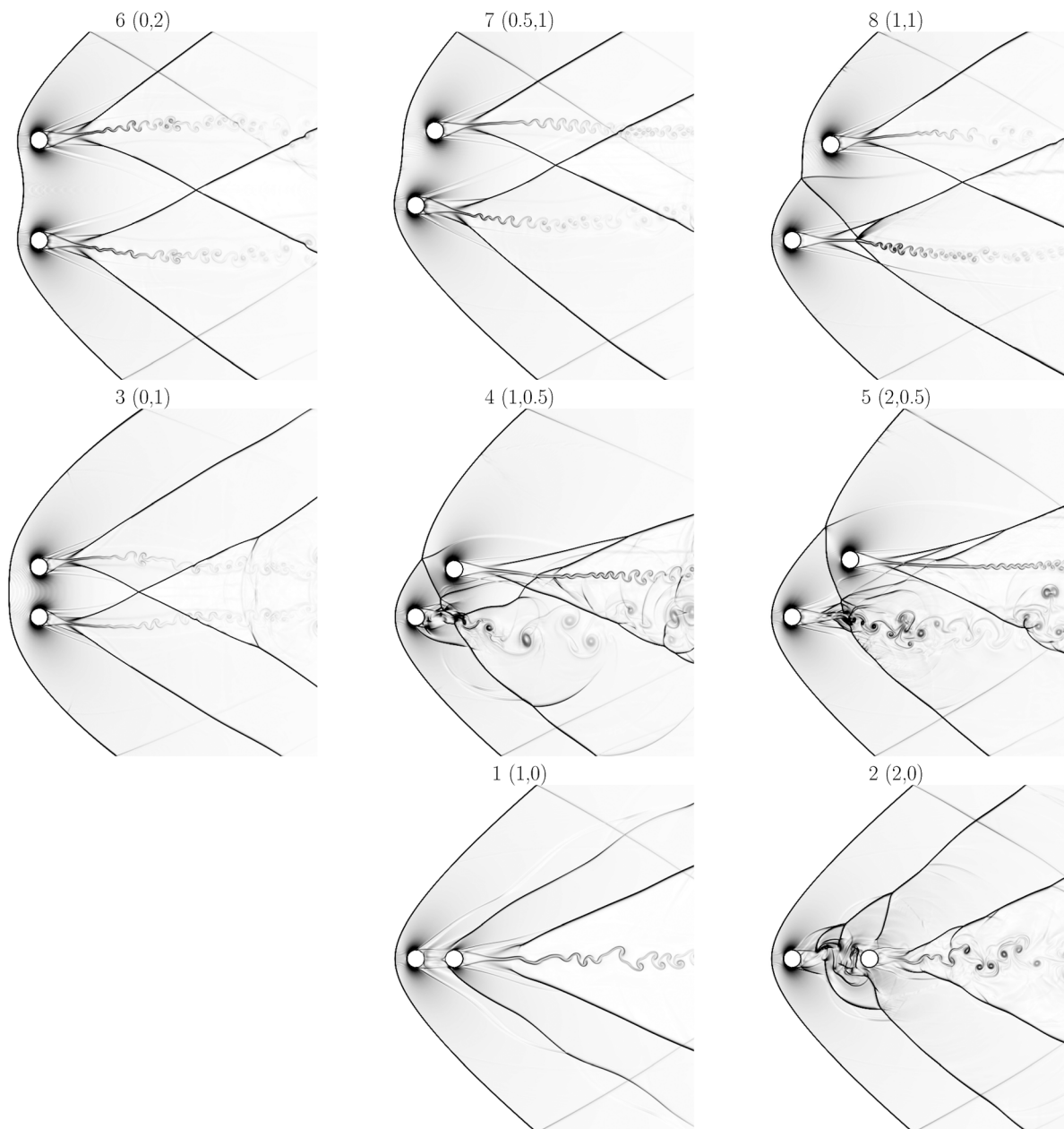


FIG. 7. Numerical Schlieren for binary body arrangements at $M = 2$.

However, the secondary body positions are such that shock interactions occur far from the body. Small changes in relative body position may produce Edney type IV or type I.

2. Surface properties

Figures 10–12 show the surface pressure, skin friction and heat transfer coefficients. Both C_p and C_f profiles imply the forces acting on the bodies, and C_h implies the total heat load. The results show that:

- Often C_p is symmetrical, which means there is no net lift and only a drag force on the body; whereas an asymmetrical C_p profile suggests the presence of a lift force and a drag force. Furthermore, the C_p distribution is smooth, peaks at the stagnation point, and is close to zero behind the cylinder.
- Often C_f is antisymmetric. This suggests zero net torque acting on the body and only drag force due to viscosity. C_f magnitude is $100\times$ smaller than C_p and its contribution to drag is negligible. Whereas an asymmetrical profile suggests a net torque acting on

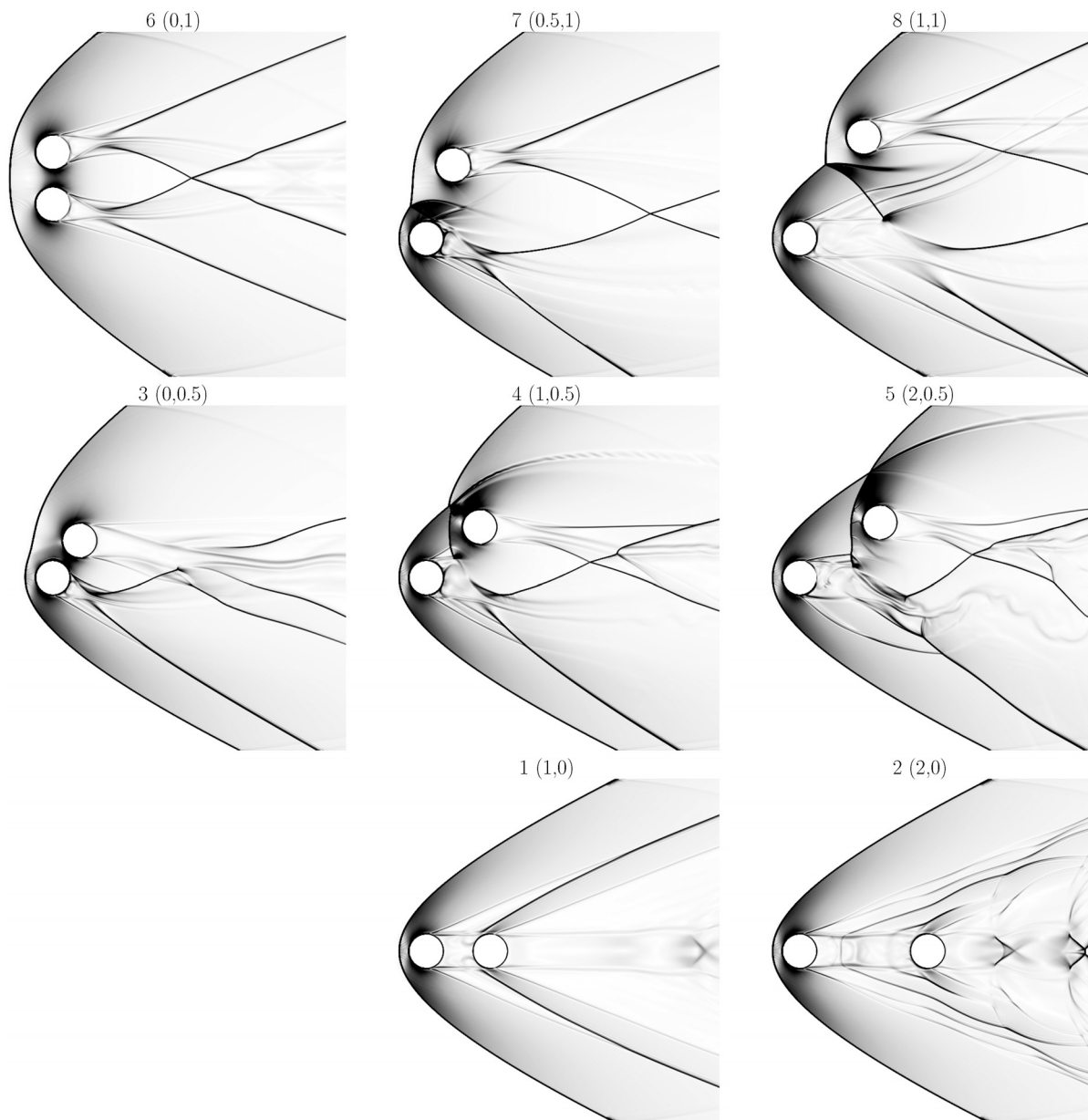


FIG. 8. Numerical Schlieren for binary body arrangements at $M = 4$.

the body. Moreover, C_f tends to zero at the stagnation point and peaks when surface tangents are aligned with the free-stream, and its local maxima and minima are due to boundary layer separations and attachments.

- A symmetrical C_h profile around the body centerline suggests similar heating on both sides of the cylinder, whereas, in an asymmetrical profile, one side is heated more than the other. C_h peaks at the stagnation point and is negligible on a surface with zero projected area (shadow surfaces) in the flow direction. The profile's asymmetry increases with increasing Mach number

while the peak heat transfer and heat load are also visibly different with the arrangements.

Figures 13(a) and 13(c) show the normalized heat load flux and the peak heat flux on both bodies in all arrangements. The results are conservatively presented to two significant figures considering mesh convergence in Sec. IV A. Overall, the normalized heat load and peak heat flux can increase up to 1.2 and decrease to 0.1. Generally, the magnitude of variation in heat load and peak heat augmentation is observed to be insensitive to the Mach number. A similar magnitude

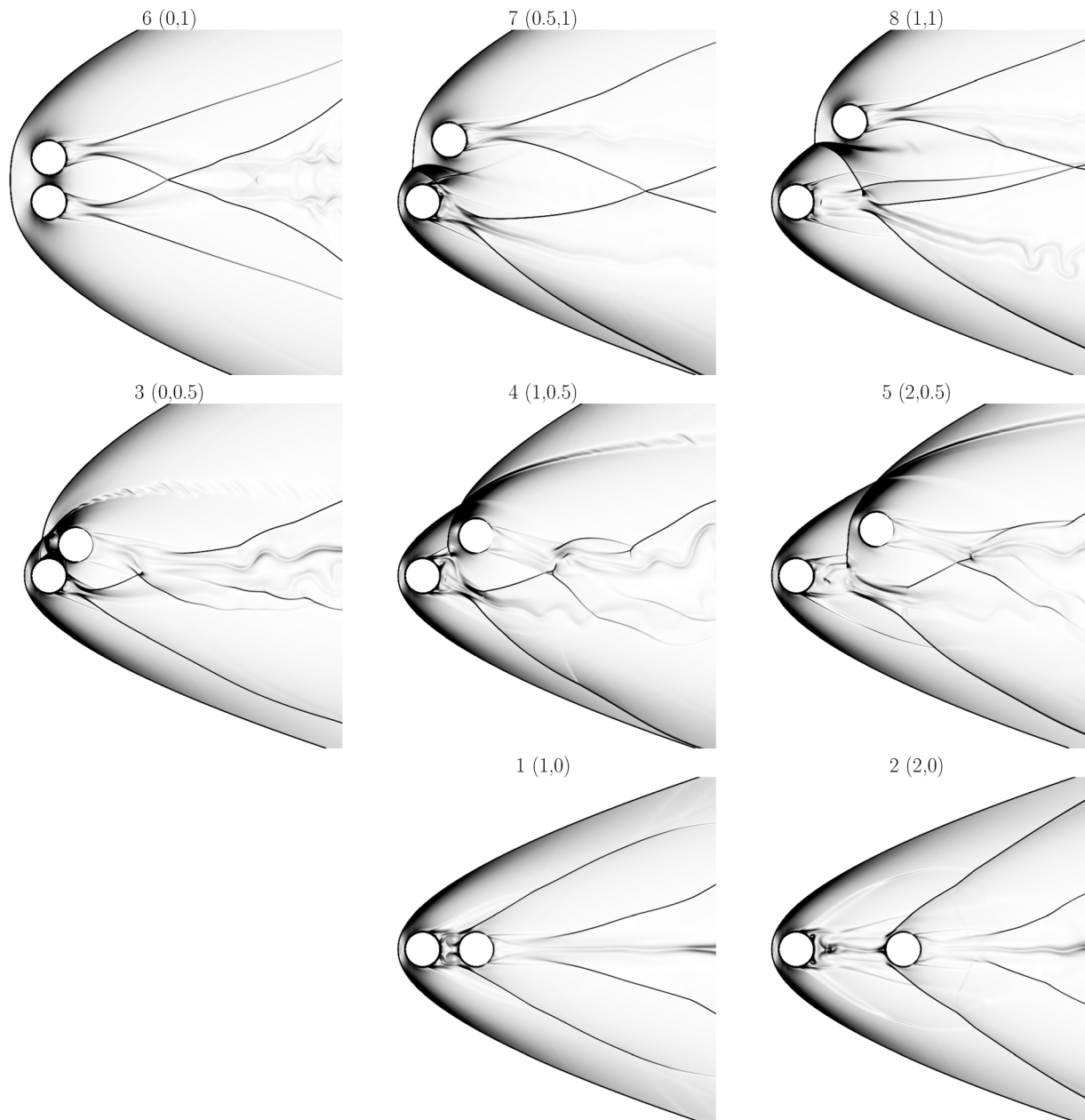


FIG. 9. Numerical Schlieren for binary body arrangements at $M = 8$.

of variation is also likely to be the case for even higher Mach numbers, and thermochemically frozen flow, as the wake topology remains similar.

When the secondary body is directly behind the primary body, it is significantly thermally shielded. The shielding is due to a reduction in heat transfer on the front half of the cylinder ($-\pi/2 < \theta < \pi/2$). This occurs in arrangements 1 and 2 for all Mach numbers, but can also be observed in arrangements 4 and 5 at $M = 8$. The heat transfer is reduced on the front half of the cylinder due to a weaker flow

impingement around the stagnation region because of shielding from the leading body. This pressure shielding can also be observed in arrangement 5 at $M = 8$.

On the other hand, the increase in heat load is due to an increase in heat transfer on the sides of the cylinder ($\pi/4 < |\theta| < 3\pi/4$), because of the hot shock layer flow being forced between the two bodies. As the secondary body moves toward the primary body's bow shock, as in arrangements 3 and 6, the heat transfer to both bodies increases.

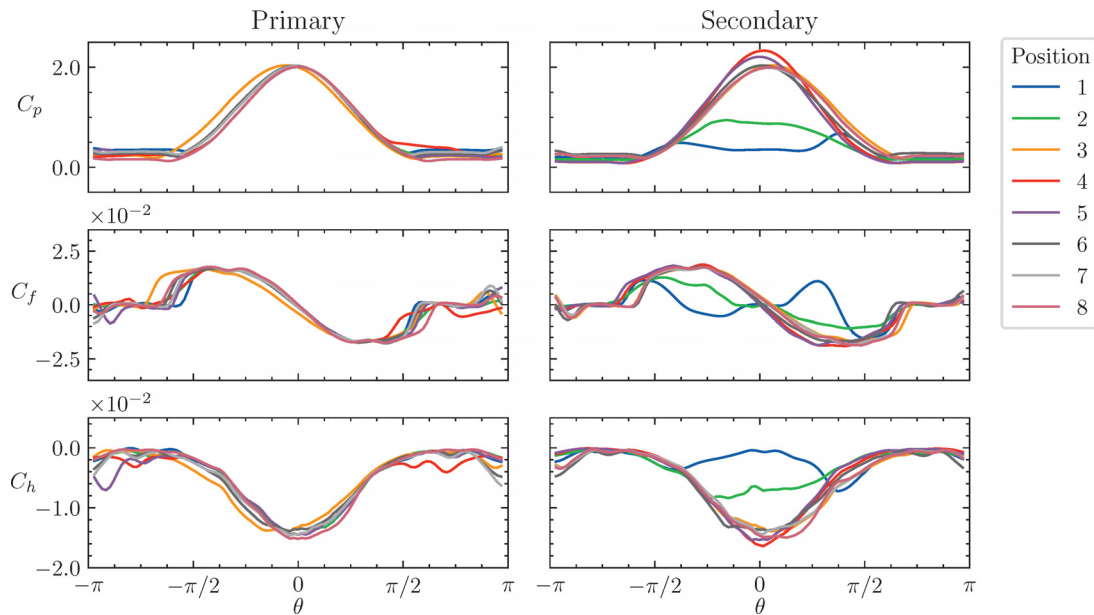


FIG. 10. Surface properties for binary body arrangements at $M=2$. θ is positive in the anti-clockwise direction. The body centerline, aligned with the free-stream, passes through $\theta = 0$.

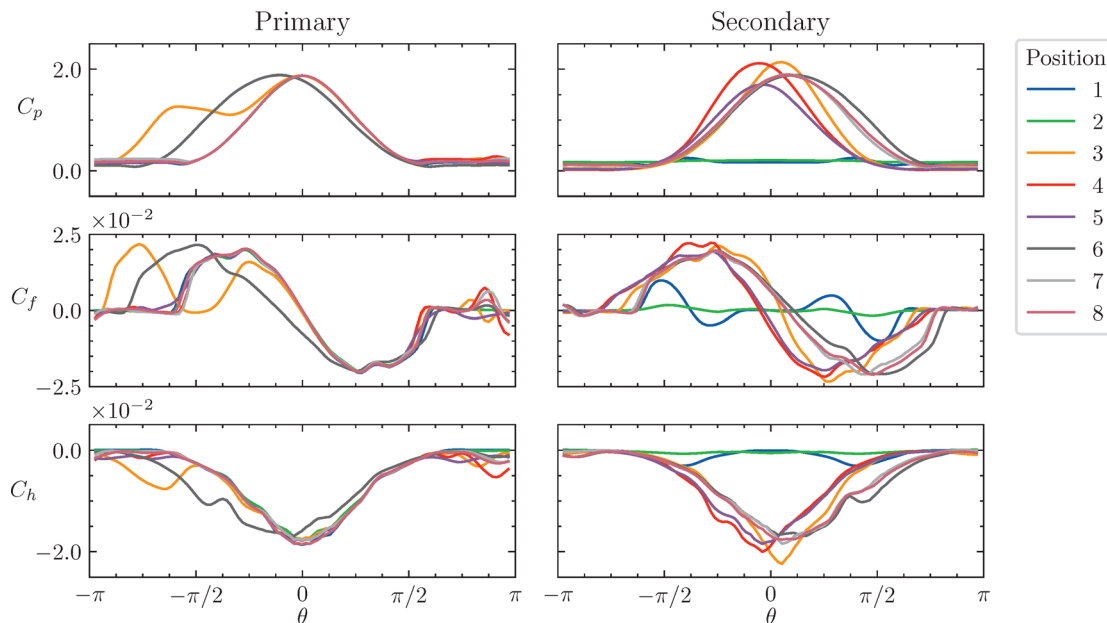


FIG. 11. Surface properties for binary body arrangements at $M=4$. θ is positive in the anti-clockwise direction. The body centerline, aligned with the free-stream, passes through $\theta = 0$.

Another observation is that arrangements 1 and 2 at $M=2$ generate larger heat loads and peak heating than at $M=4$ and $M=8$. This is because of mixing in the shock layer due to a higher wake Reynolds number at $M=2$, the mixing was also observed with the numerical Schlieren in Sec. IV B 1.

V. MULTIPLE BODIES

Following the investigation of heat transfer to binary proximal bodies, a natural first step is to consider multiple bodies, also referred to as a cluster. Many of the parameters which affect the bodies' surface properties are the same as in binary bodies, namely the flow Mach

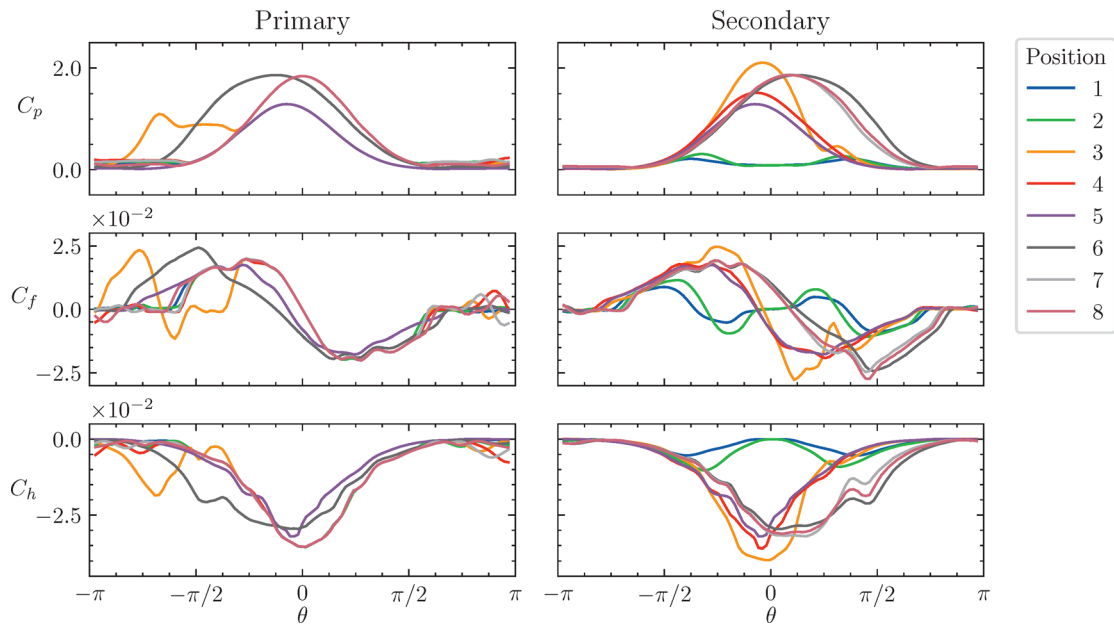


FIG. 12. Surface properties for binary body arrangements at $M=8$. θ is positive in the anti-clockwise direction. The body centerline, aligned with the free-stream, passes through $\theta = 0$.

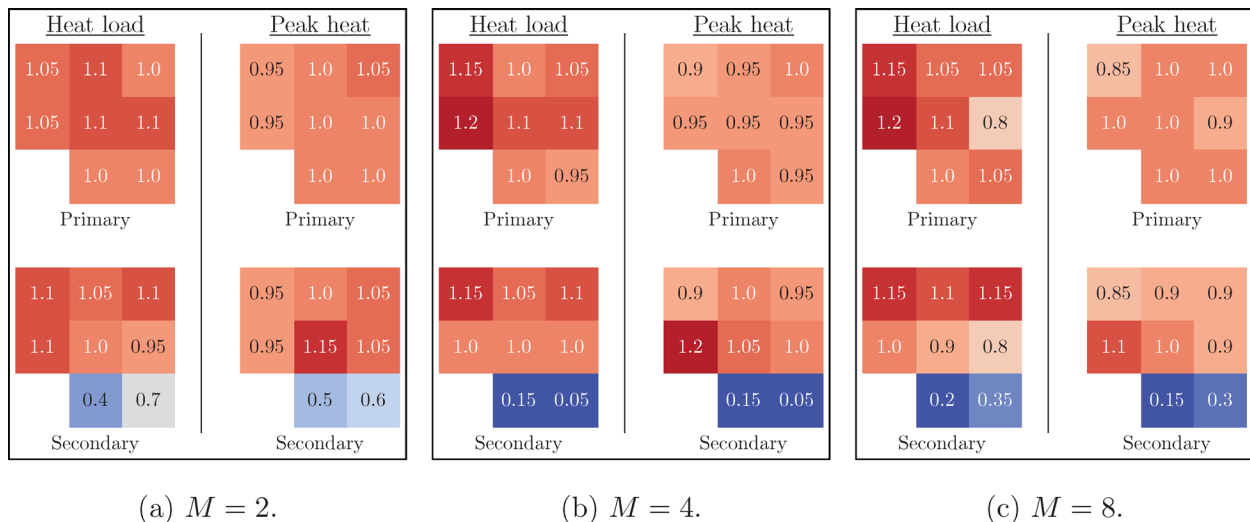


FIG. 13. Heat load and peak heat flux for binary body arrangements, normalized by the heat load and the stagnation point heat flux to an isolated body. Same order as in Figs. 7–9.

number and Reynolds number. However, with multiple bodies, the number of bodies in a cluster and the size and position of the bodies widen the parameter space. In this study, the focus is only on the effect of body positions on heat transfer. Only one flow condition with free-stream at $M = 4$ and $Re = 10\,000$; and clusters of five equal-sized bodies at the specified flow conditions are considered.

The clusters are generated by randomly placing cylinder centers while ensuring no overlap with each other, and that the bodies are

located within the computational domain. Eight positions are selected, see arrangements in Appendix B. The variety in the spatial arrangement of the bodies in the cluster is ensured: cases 7 and 8 are closely arranged; 1 and 2 are medium distance apart; 5 and 6 are loosely arranged; and 3 and 4 are arranged roughly linearly—horizontally and vertically. The numerical setup is identical to the $M = 4$ binary body study in Sec. IV B. Figure 14 shows the instantaneous mesh for cases 2 and 5.

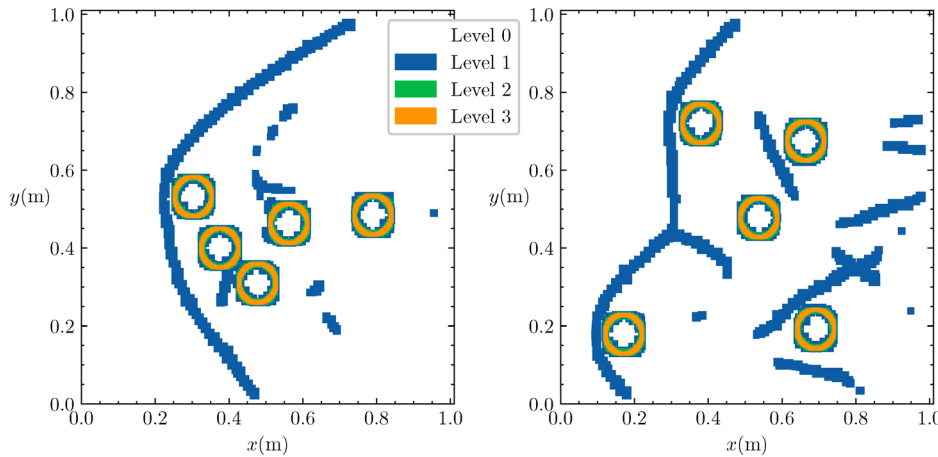


FIG. 14. Cases 2 (left) and 5 (right) instantaneous AMR mesh with three levels of refinement around the bodies and one level of refinement around shocks.

Let $h_{ij}(\theta)$ be the local time varying heat transfer for body i in a given cluster at time j ,

$$Q_{ij} = \int_0^{2\pi} h_{ij}(\theta) d\theta, \quad \bar{Q}_i = \frac{\sum_j Q_{ij}}{N_t}, \quad \langle \bar{Q} \rangle = \sum_i \frac{\bar{Q}_i}{N_b},$$

$$\sigma\{\bar{Q}\} = \left(\sum_i \frac{(\bar{Q}_i - \langle \bar{Q} \rangle)^2}{N_b} \right)^{1/2}$$

where N_b is the number of bodies in a cluster, N_t is the number of samples at different times, Q_{ij} is the heat load for body i and time j , \bar{Q}_i is the time-averaged heat load for body i in a cluster, $\langle \bar{Q} \rangle$ is the time- and cluster-averaged heat load and $\sigma\{\bar{Q}\}$ is the standard deviation of the time-averaged heat load over bodies in a cluster. The heat transfer coefficient C_h is averaged similarly.

A. Numerical Schlieren

Figure 15 shows the instantaneous numerical Schlieren image from the eight cases, where the five bodies are labeled according to Table IV. The primary bow shock shape varies dramatically depending on the body arrangements, and highly unsteady wakes are generated with shock interactions and shocklet shedding. The unsteadiness is significant compared to binary body arrangements in Fig. 8 at the same free-stream conditions.

B. Averaged heat transfer

Figure 16 shows the cluster-averaged unsteady evolution heat load and heat load for each body. The flow field observed in Fig. 15 results in unsteady heat transfer to many bodies. A time-average over five flow times is deemed to be a reasonable approximation of the steady-state heat load. However, in some cases, such as Body D in case 5, the current sampling frequency of 0.5 flow time may not be sufficient for an accurate time-average. This is unlikely to change the qualitative trends.

Figure 16 indicates that the maximum time-averaged heat load on a given body is around 1.4 (body 8A), compared to a factor of 1.2 in the binary bodies configuration. While the minimum heat load is

around 0.1 (body 3B), same as in the binary bodies. The figure also shows that some bodies experience significant unsteadiness. Case 5 has the largest heat load fluctuations (0.2 peak-to-peak). In contrast, all bodies in cases 4 and 7 experience a steady heat load. In the remaining cases—1, 2, 3, 6, and 8—only some bodies experience an unsteady heat load. Bodies C and E in case 6 experience unsteady heat load whereas bodies A, B, and E undergo steady heating. Finally, an important observation is that the normalized cluster and time-averaged heat load approximately varies between 1.2 and 0.4.

Figure 17 shows the time-averaged heat transfer coefficient for all cases. The normalized maximum peak heat flux is around 1.4 larger (on body 2C), and the minimum is 0.2 (case 2E). This suggests a large variation in peak heating occurs on bodies in a given cluster. Comparatively, binary body configurations produced peak heating in the range of 1.2–0.1. All peaks occur between $-\pi/2 < \theta < \pi/2$, on the front half of the cylinders, as expected. Large spatial variations occur in case 8; whereas cases 1, 2, 4, and 7 have medium variations; and 3 and 6 have small variations. Overall, the additional heating on the sides and back of the cylinders is the cause of the increased heat load.

Figure 18 shows the time- and cluster-averaged coefficient of heat transfer, $\langle \bar{C}_h \rangle$, profiles around the cylinder for all the cases considered. All cases have their average stagnation-point heat transfer reduced by around 10%–50% compared to an isolated body. This is because some bodies are shielded from the direct shocked flow, for example, some bodies in cases 1, 2, 3, and 7. These shielded bodies have a reduced heat load around the stagnation region. However, the heat transfer around the sides and the back, for $\pi/4 \leq |\theta| < \pi$, is increased in many cases. This increase not only offsets the reduction in heat load around the stagnation region but also results in a net increased heat load when compared to an isolated body.

C. Cluster-averaged heat load

Figure 19 shows the magnitude of normalized cluster-average heat load, which can also be inferred from Fig. 16. It shows that bodies on average, in cases 4, 5 and 8, receive a larger heat load than an isolated body ($\langle \bar{Q} \rangle / Q_1 > 1$). In case 5, the unsteadiness and mixing in the wake are responsible for the increased heat load, as suggested by Fig. 16. However, in case 4, where the flow is steady, additional heating

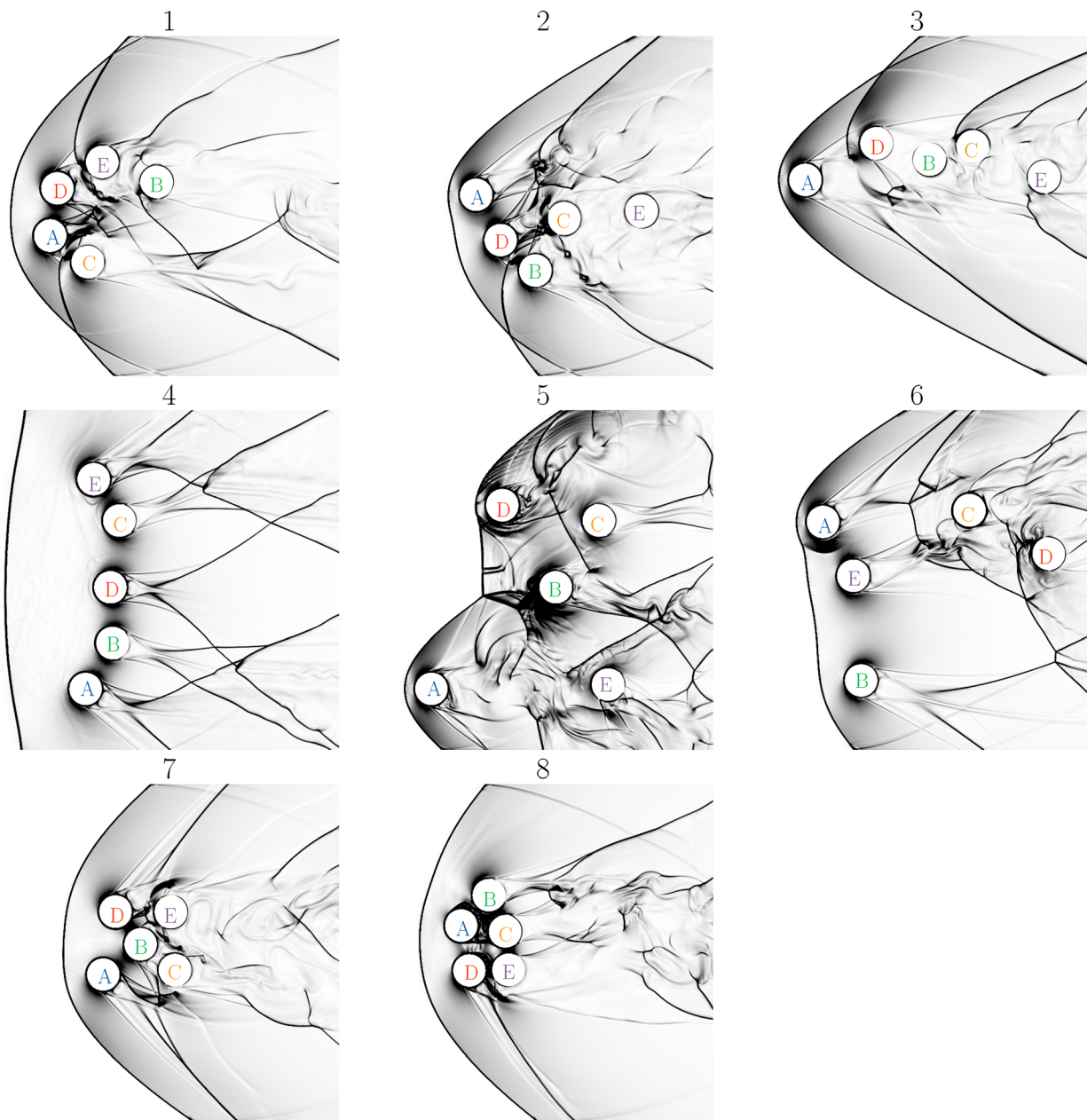


FIG. 15. Numerical Schlieren of the eight, five-body clusters at $M = 4$. Where the bodies are labeled from A to E.

is due to the flow being forced to pass between the cylinders—as suggested by Figs. 16 and 17. In contrast, case 8 has increased heating on the side and back, as the hot gases from the stagnation region of the combined bow shock linger in the small spaces in between the bodies—as suggested by Fig. 17. Overall, the increase in time- and cluster-averaged heat load seems to be caused by different mechanisms. On the other hand, cases 1, 2, 3, and 7 are subject to a reduced heat load ($\langle \bar{Q} \rangle / Q_1 < 1$). This occurs because some bodies are shielded from the direct shock layer flow and are in the cooler viscous wake of another

body, as seen in Fig. 15. Such shielded bodies have reduced heat transfer around their stagnation region, as shown in Fig. 18. Moreover, the heat load in case 6 is on average the same as an isolated body ($\langle \bar{Q} \rangle / Q_1 \approx 1$), as the increase in heat transfer to the leading bodies is negated by the reduced heat transfer to the trailing bodies. Finally, bodies in cases 7 and 8 are arranged in a visually similar manner, but they differ in their normalized average heat load: 1.2 and 0.85, respectively. Figures 16 and 17 suggest that case 8 is more unsteady and receives larger heating on the sides and back than case 7.

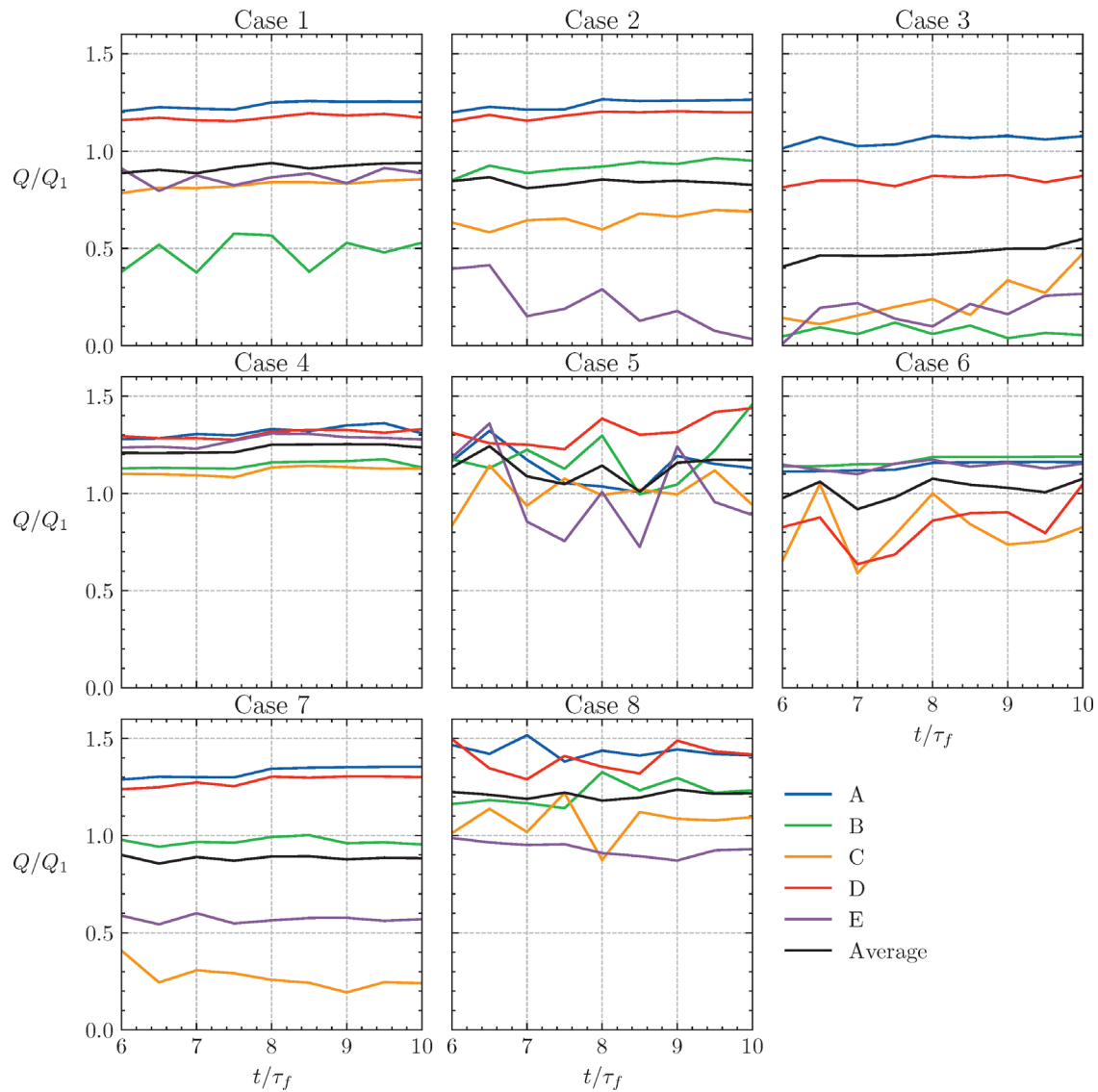


FIG. 16. Normalized heat load (\bar{Q}/Q_1) varying over 6–10 flow times (t/τ_f) for all bodies, in all cases. Where Q_1 is the heat load to an isolated body and τ_f is the flow time based on domain length and free-stream velocity.

Figure 19 also shows the scaling of normalized time- and cluster-averaged heat load with cluster geometrical properties. Simple properties like the standard deviation of the body positions in both coordinate directions give good correlations with current cases. More complex properties like projected area in the flow direction, and for a collection of points (body centers) Hamiltonian path, Minkowski distance, did not give improved correlations. The standard deviation of the coordinate parallel to the flow vector ($\sigma\{x\}$) and perpendicular to the flow vector ($\sigma\{y\}$) correlate well with the time- and cluster-averaged heat load. However, the ratio $\sigma\{x\}/\sigma\{y\}$ correlates the best.

Overall, the correlations suggest that increasing $\sigma\{x\}$ decreases the time- and cluster-averaged heat load. In contrast, $\sigma\{y\}$ is directly

proportional to time- and cluster-averaged heat load. Importantly, it suggests that when $\sigma\{x\}/\sigma\{y\} \geq 1$, the average heat load is less than compared to an isolated body; in other words, thermal shielding occurs. Alternatively, when $\sigma\{x\}/\sigma\{y\} \leq 1$, the average heat load is more than an isolated body; in other words, thermal amplification occurs.

Note, these correlations are only valid for closely packed clusters with $\sigma\{x\} \leq 3D$ and $\sigma\{y\} \leq 3D$. For $\sigma\{y\} \gg 3D$, meaning the bodies in the cluster are far apart and are essentially isolated. Therefore, the current linearly increasing heat load behavior cannot be sustained for all values of $\sigma\{y\}/D$.

Figure 20 shows the time-averaged heat load standard deviation in a cluster, correlated with four parameters. The strongest (negative)

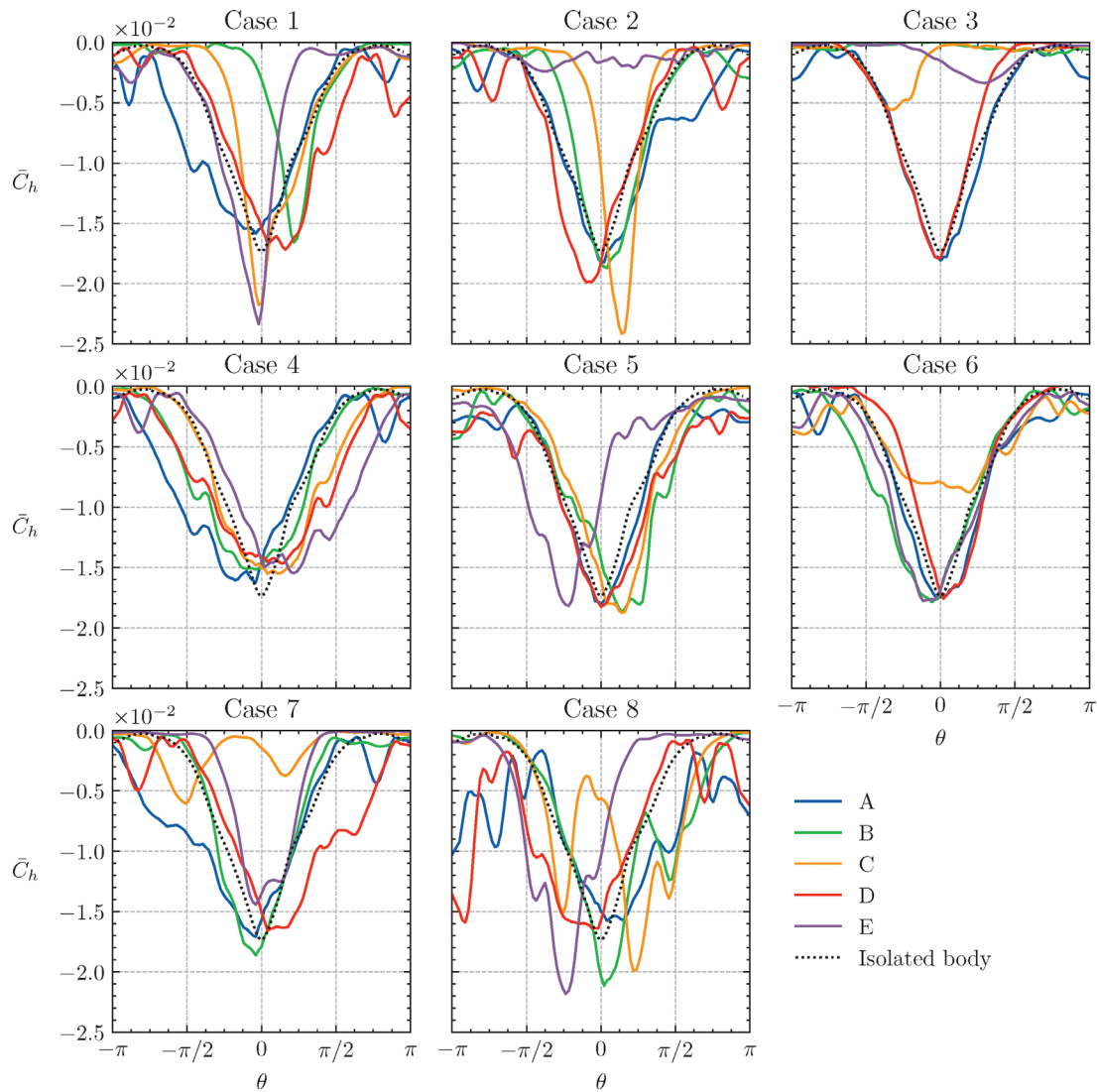


FIG. 17. Time-averaged heat transfer coefficient (\bar{C}_h) profiles for each body in each case, compared with an isolated body. θ is positive in the anti-clockwise direction.

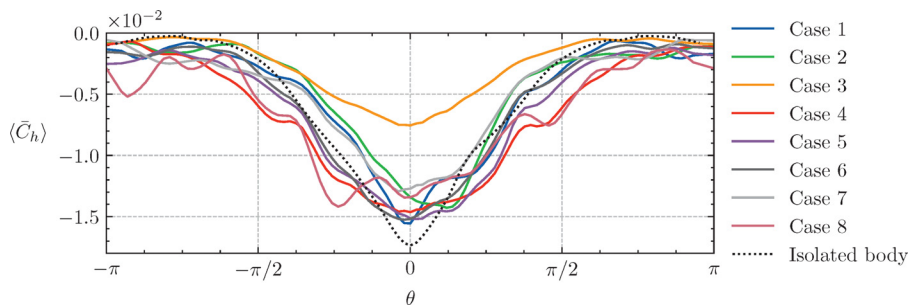


FIG. 18. Time- and cluster-averaged heat transfer coefficient ($\langle \bar{C}_h \rangle$) profiles for all cases. θ is positive in the anti-clockwise direction.

correlation is observed with $\sigma\{y\}$ and the weakest positive correlation is with $\sigma\{x\}$. Note, increasing $\sigma\{y\}$ cannot decrease $\sigma\{Q\}$ beyond 0. Intuitively, the heat load variance must go to zero as the cluster size increases and the bodies become isolated. This means that for

$\sigma\{y\} \geq 3D$, there must be a change in trend. Moreover, $\sigma\{x\}/\sigma\{y\}$ shows a positive correlation; and $\langle \bar{Q} \rangle / Q_1$ shows a negative correlation. This means that heated clusters have a smaller variation of heat load among their bodies than cooled clusters.

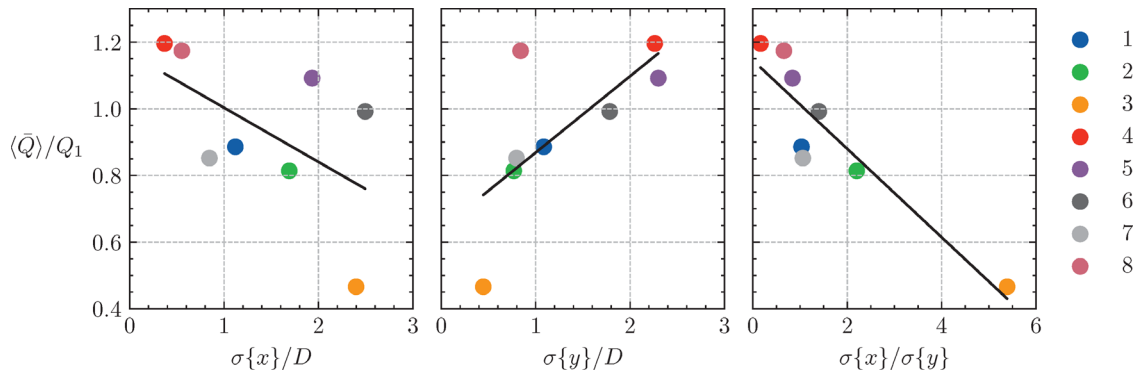


FIG. 19. Normalized time- and cluster-averaged heat load ($\langle \bar{Q} \rangle / Q_1$) scaling with normalized body position standard deviations ($\sigma\{x\}/D$, $\sigma\{y\}/D$, $\sigma\{x\}/\sigma\{y\}$) for all cases.

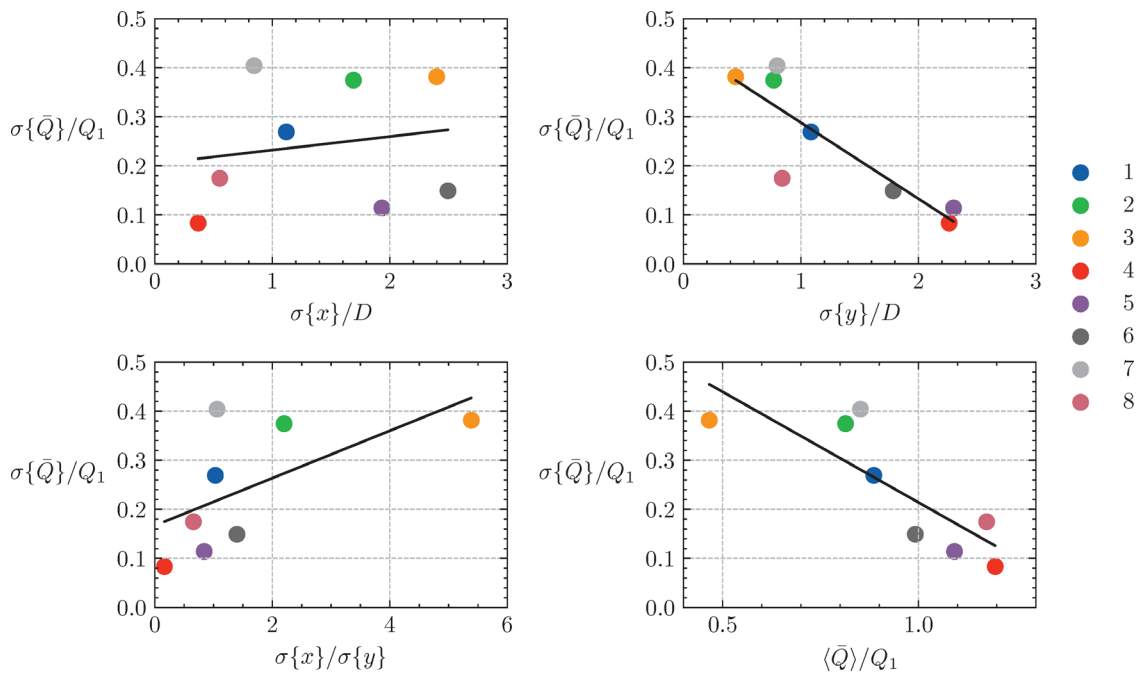


FIG. 20. Normalized time-averaged heat load standard deviation ($\sigma\{\bar{Q}\}/Q_1$) scaling with, normalized body position standard deviations ($\sigma\{x\}/D$, $\sigma\{y\}/D$, $\sigma\{x\}/\sigma\{y\}$) and ensemble time-average heat load ($\langle \bar{Q} \rangle / Q_1$) for all cases.

VI. CONCLUSION

This paper studied the heat transfer in proximal cylinders in the near wake at Mach numbers 2, 4, and 8, with constant wall temperature, under the calorically perfect gas assumption. First, binary bodies are considered, where the secondary body’s positions are systematically varied in the primary body’s near wake. The key findings are as follows:

- The heat load and peak heat transfer can be augmented for either one or both proximal bodies by +20% to −90% of an isolated body. The magnitude of variation in the heat load and the peak heat transfer seems insensitive to the Mach numbers investigated. Moreover, this trend is expected to continue in flows with larger Mach numbers than investigated, in frozen flow and given a similar free-stream Reynolds number.

- Minimum heat load and minimum peak heat transfer (maximum thermal shielding) occur when the secondary body is in the viscous wake of the primary body. The thermal shielding is due to a reduction in heat transfer to the front half of the cylinder due to a weaker flow impingement, because of flow shielding from the leading body.
- Maximum heat load and peak heat flux occur when the secondary body approaches the primary body’s bow shock and stagnation region. The increase in heat load is due to increased heat transfer around the sides of the cylinder ($\pi/4 < |\theta| < 3\pi/4$) due to the hot shock layer gases being forced to pass between the two bodies.

Second, multiple bodies near each other are considered. Eight clusters with five randomly arranged cylinders are selected, and the

02 January 2025 11:35:46

cluster-average heat transfer and standard deviation are described and found to correlate well with cluster geometrical properties. The key findings are:

- The maximum time-averaged heat load on a given body in a cluster can vary between around +40% to −90% compared to an isolated body. The increase in heat load is mainly from additional heating to the sides and the back of the cylinders, whereas the decrease is mainly due to reduced heat transfer on the front half of the cylinder. Moreover, flow fields can be highly unsteady, resulting in unsteady heat transfers.
- The time- and cluster-averaged heat load in a cluster varies between +20% and −60% of an isolated body. The change in heat load among the clusters is mainly due to the change in heat transfer around the sides and the back. The average heat load around the stagnation region is also reduced in most clusters, as the following bodies are shielded by the leading bodies from the direct flow. The increased heat transfer to the sides and back is caused by: unsteadiness and mixing in the wake; the flow being forced in between the cylinders; or the hot flow from the stagnation region lingering in the small spaces in between the bodies.
- The time- and cluster-averaged heat load in a cluster shows a strong negative correlation with the ratio of the standard deviation of body coordinates in the direction parallel to the free-stream velocity to the deviation of body coordinates in the perpendicular direction. In other words, clusters thin in the direction perpendicular to the free-stream velocity and long in the direction parallel to the free-stream velocity have their heat load reduced (thermally shielded) while thick and short clusters have an increased heat load.
- The time-averaged heat load standard deviation in a cluster shows a negative correlation with the magnitude of the time- and cluster-averaged heat load. This means that heated clusters have a smaller variation of heat load among their bodies than cooled clusters.

Despite the current limitation of this study to two-dimensional flows, the trends and intuition gained in the current work are likely to apply to three-dimensional flows, at least qualitatively. Future works should investigate heat transfer to proximal bodies in three-dimensions and the effect of thermochemical relaxation, which could have large effects on heat transfer. Also, the effect of the wake Reynolds number on the heat transfer, particularly in the far wake, should also be investigated.

TABLE IV. Cylinder center coordinates (x, y) (m) for each case.

Case	A	B	C	D	E
1	(0.150, 0.413)	(0.463, 0.570)	(0.260, 0.335)	(0.171, 0.551)	(0.303, 0.629)
2	(0.303, 0.532)	(0.477, 0.310)	(0.562, 0.463)	(0.375, 0.400)	(0.790, 0.485)
3	(0.171, 0.576)	(0.537, 0.636)	(0.664, 0.675)	(0.380, 0.684)	(0.874, 0.585)
4	(0.254, 0.179)	(0.333, 0.314)	(0.353, 0.675)	(0.327, 0.478)	(0.278, 0.796)
5	(0.171, 0.179)	(0.537, 0.478)	(0.664, 0.675)	(0.380, 0.720)	(0.691, 0.192)
6	(0.223, 0.671)	(0.335, 0.204)	(0.654, 0.705)	(0.887, 0.577)	(0.312, 0.512)
7	(0.306, 0.439)	(0.416, 0.528)	(0.517, 0.452)	(0.342, 0.624)	(0.505, 0.623)
8	(0.259, 0.583)	(0.340, 0.672)	(0.388, 0.566)	(0.283, 0.451)	(0.398, 0.453)

ACKNOWLEDGMENTS

The authors would like to thank and acknowledge P. Bruce for his comments on the work. The authors also acknowledge Engineering and Physical Sciences Research Council (EPSRC) (No. EPSRC-DTP 2018/19) and Mechanical Engineering Department at Imperial College London for the funding.

AUTHOR DECLARATIONS

Conflict of Interest

The authors have no conflicts to disclose.

Author Contributions

Monal Patel: Conceptualization (lead); Data curation (lead); Formal analysis (lead); Investigation (lead); Methodology (equal); Project administration (equal); Software (equal); Validation (equal); Visualization (equal); Writing – original draft (lead); Writing – review & editing (lead). **Salvador Navarro-Martinez:** Funding acquisition (equal); Project administration (equal); Resources (equal); Software (equal); Supervision (equal); Writing – review & editing (supporting).

DATA AVAILABILITY

The data that support the findings of this study are available from the corresponding author upon reasonable request.

APPENDIX A: FLOW LENGTH SCALES

Flow length scales, estimated from the mesh refinement study, are summarized in Table III. These values are used to calculate the positions of the second cylinder in real space from non-dimensional space, as illustrated in Fig. 3.

TABLE III. Flow length scales at different Mach numbers. The length scales are rear stagnation-point distance (l_s) and bow shock transverse distance (y_s).

M	l_s (m)	$y_s(\hat{x} = 0)$	$y_s(\hat{x} = 0.5)$	$y_s(\hat{x} = 1)$	$y_s(\hat{x} = 2)$
2	0.222	0.288	0.430	0.550	1.250
4	0.186	0.148	0.228	0.292	0.404
8	0.155	0.128	0.180	0.232	0.311

APPENDIX B: MULTIPLE BODIES CASES

The body positions for each case in Sec. V are listed in Table IV.

REFERENCES

- ¹P. Register, M. Aftosmis, E. Stern, J. Brock, P. Seltner, S. Willems, A. Gülhan, and D. Mathias, "Interactions between asteroid fragments during atmospheric entry," *Icarus* **337**, 113468 (2020).
- ²Q. R. Passey and H. Melosh, "Effects of atmospheric breakup on crater field formation," *Icarus* **42**, 211–233 (1980).
- ³T. Lips and B. Fritsche, "A comparison of commonly used re-entry analysis tools," *Acta Astronaut.* **57**, 312–323 (2005).
- ⁴B. E. Edney, "Effects of shock impingement on the heat transfer around blunt bodies," *AIAA J.* **6**, 15–21 (1968).
- ⁵B. Edney, "Anomalous heat transfer and pressure distributions on blunt bodies at hypersonic speeds in the presence of an impinging shock," Report No. FFA-115 (Flygtekniska Forsöksanstalten, Stockholm, Sweden, 1968).
- ⁶J. W. Keyes and F. D. Hains, "Analytical and experimental studies of shock interference heating in hypersonic flows," Report No. NASA-TN-D-7139 (NASA, 1973).
- ⁷S. J. Laurence, R. Deiterding, and G. Hornung, "Proximal bodies in hypersonic flow," *J. Fluid Mech.* **590**, 209–237 (2007).
- ⁸A. Marwege, S. Willems, A. Gülhan, M. J. Aftosmis, and E. C. Stern, "Superposition method for force estimations on bodies in supersonic and hypersonic flows," *J. Spacecr. Rockets* **55**, 1166–1180 (2018).
- ⁹S. J. Laurence, N. J. Parziale, and R. Deiterding, "Dynamical separation of spherical bodies in supersonic flow," *J. Fluid Mech.* **713**, 159–182 (2012).
- ¹⁰S. J. Laurence and R. Deiterding, "Shock-wave surfing," *J. Fluid Mech.* **676**, 396–431 (2011).
- ¹¹S.-H. Park, J. Kim, I. Choi, and G. Park, "Experimental study of separation behaviour of two bodies in hypersonic flow," *Acta Astronaut.* **181**, 414–426 (2021).
- ¹²S.-H. Park and G. Park, "Separation process of multi-spheres in hypersonic flow," *Adv. Space Res.* **65**, 392–406 (2020).
- ¹³T. J. Whalen and S. J. Laurence, "Experiments on the separation of sphere clusters in hypersonic flow," *Exp. Fluids* **62**, 70 (2021).
- ¹⁴C. Sousa, R. Deiterding, and S. J. Laurence, "Dynamics of a spherical body shedding from a hypersonic ramp—Part 1: Inviscid flow," *J. Fluid Mech.* **906**, A28 (2021).
- ¹⁵C. Butler, T. Whalen, C. Sousa, and S. Laurence, "Dynamics of a spherical body shedding from a hypersonic ramp—Part 2: Viscous flow," *J. Fluid Mech.* **906**, A29 (2021).
- ¹⁶W. S. Hinman and C. T. Johansen, "Mechanisms in the hypersonic laminar near wake of a blunt body," *J. Fluid Mech.* **839**, 33–75 (2018).
- ¹⁷L. Wilson, "Far wake behavior of hypersonic spheres," *AIAA J.* **5**, 1238–1244 (1967).
- ¹⁸W. Behrens, "The far wake behind cylinders at hypersonic speeds—I," *AIAA J.* **5**, 2135–2141 (1967).
- ¹⁹L. Lees, "Hypersonic wakes and trails," *AIAA J.* **2**, 417–428 (1964).
- ²⁰F. R. Hama, "Experimental studies on the lip shock," *AIAA J.* **6**, 212–219 (1968).
- ²¹J. A. Fay and F. R. Riddell, "Theory of stagnation point heat transfer in dissociated air," *J. Aerosp. Sci.* **25**, 73–85 (1958).
- ²²J. D. Anderson, Jr., *Hypersonic and High-Temperature Gas Dynamics* (American Institute of Aeronautics and Astronautics, 2006).
- ²³M. E. Tauber, "A review of high-speed, convective, heat-transfer computation methods," NASA Report No. 2914 (1989).
- ²⁴E. Touber and N. Alferéz, "Shock-induced energy conversion of entropy in non-ideal fluids," *J. Fluid Mech.* **864**, 807–847 (2019).
- ²⁵Y. Almeida and S. Navarro-Martinez, "Large eddy simulation of supersonic combustion using the Eulerian stochastic fields method," *Flow, Turbul. Combust.* **103**, 943–962 (2019).
- ²⁶M. Patel, "Hypersonic flows around complex geometries with adaptive mesh refinement and immersed boundary method," Ph.D. thesis (Imperial College London, 2023).
- ²⁷See <https://github.com/BoxLib-Codes/BoxLib> for J. Bell, A. Almgren, V. Beckner, M. Day, M. Lijewski, A. Nonaka, and W. Zhang, "BoxLib GitHub repository," accessed 01-03-2021 (2014).
- ²⁸F. Ducros, F. Laporte, T. Soullères, V. Guinot, P. Moinat, and B. Caruelle, "High-order fluxes for conservative skew-symmetric-like schemes in structured meshes: Application to compressible flows," *J. Comput. Phys.* **161**, 114–139 (2000).
- ²⁹C.-W. Shu and S. Osher, "Efficient implementation of essentially non-oscillatory shock-capturing schemes," *J. Comput. Phys.* **77**, 439–471 (1988).
- ³⁰D. T. Britt and G. Consolmagno, "Stony meteorite porosities and densities: A review of the data through 2001," *Meteorit. Planet. Sci.* **38**, 1161–1180 (2003).